Journal of Alloys and Compounds 466 (2008) 119–125

Journal of ALLOYS AND COMPOUNDS

www.elsevier.com/locate/jallcom

The stress relaxation of a $Fe_{59}Mn_{30}Si_6Cr_5$ shape memory alloy

H.C. Lin [a,*], T.P. Wang [b], K.M. Lin [b], C.Y. Chung [b], P.C. Wang [a], W.H. Ho [c]

[a] Department of Materials Science and Engineering, National Taiwan University, Taipei, Taiwan
[b] Department of Materials Science and Engineering, Feng Chia University, Taichung, Taiwan
[c] Department of Product Development, Taiwan Textile Research Institute, Taipei, Taiwan

Received 6 July 2007; received in revised form 12 November 2007; accepted 12 November 2007
Available online 22 November 2007

Abstract

The relaxation phenomena arising from both the static-constrained stress and the cyclic variation of atmospheric temperature of $Fe_{59}Mn_{30}Si_6Cr_5$ shape memory alloy were studied. Experimental results show that the amount of relaxation decreases with increasing initial compressive loading. The cyclic variation of atmospheric temperature has a smaller effect on the relaxation than the static-constrained stress does. The relaxation phenomenon is more obvious both in the earlier cycles and at higher cyclic heating temperatures. The static-constrained stress relaxation is ascribed to the combination and rearrangement of the stress-induced thin platelets of ε martensite. The contribution of cyclic heating on the stress relaxation originates from the formation of new-oriented ε martensite. The $\varepsilon \leftrightarrow \gamma$ transformation, thermal stress and shape-recovery stress during the thermal cycling are considered to have significant influences on the formation of new-oriented ε martensite.

Keywords: $Fe_{59}Mn_{30}Si_6Cr_5$ shape memory alloy; Compressive stress relaxation; Thermal cycling

1. Introduction

In light of their low cost and excellent workability, the Fe-based shape memory alloys, which are composed of Fe–Mn–Si compositions, have attracted much attention recently. For example, the Fe–Mn–Si alloys, which contain 28–34 wt% Mn and 4–6.5 wt% Si, exhibit a nearly perfect shape memory effect (SME) [1–4]. The addition of Cr to the Fe–Mn–Si alloys improves their SME and corrosion resistance [5,6]. In contrast to the TiNi and Cu-based shape memory alloys, the Fe–Mn–Si–Cr alloys exhibit a non-thermoelastic martensitic transformation. Their SME arises from the reverse transformation of stress-induced ε martensite (HCP structure) into γ parent austenite (fcc structure) upon heating [1]. In the past decade, extensive studies of the Fe–Mn–Si–Cr alloys were made focusing on the transformation behavior [1,7–9], physical properties [7–10], effects of thermo-mechanical training [11–14] and composition dependence of SME and corrosion resistance [5,15–21]. Also, effort is made to increase the use of these alloys, especially the “heat-to-shrink” pipe coupling [22]. The fitting technique by using these alloys is a brand-new method to connect engineering pipes. It exhibits much merit than conventional welding and can be widely applied in various engineering fields. However, some problems of Fe–Mn–Si–Cr shape memory alloys should still be investigated and resolved, such as, the stress relaxation phenomena due to the long-time sustaining of constrained stress and cyclic variation of atmospheric temperature. These features will reduce the usage life of the fitting pipes and impede their applications. Hence, the understanding of the stress relaxation phenomena of Fe–Mn–Si–Cr alloys is important. In the present study, we aim at investigating the stress relaxation systematically by simulating the compressive stress state in the application of pipe fitting. The relaxation phenomena arising from both the long-time sustaining of constrained stress and the cyclic variation of atmospheric temperature are studied. Meanwhile, the variation of microstructures during the stress relaxation will also be discussed.

2. Experimental procedure

A vacuum melting technique was employed to prepare the $Fe_{59}Mn_{30}Si_6Cr_5$ (wt%) alloy. The as-cast ingot was homogenized at 1200 °C for 24 h, hot-rolled at 1200 °C into 35 mm-thickness plate and then annealed at 1200 °C for 1.5 h. Specimens with dimensions of Ø 10 mm × L15 mm were carefully cut from this plate using a CNC wire electro-discharge machine. The experiments of stress

* Corresponding author. Tel.: +886 2 3366 4532; fax: +886 2 2363 4562.
E-mail address: hclinntu@ntu.edu.tw (H.C. Lin).

0925-8388/$ – see front matter © 2007 Elsevier B.V. All rights reserved.
doi:10.1016/j.jallcom.2007.11.068

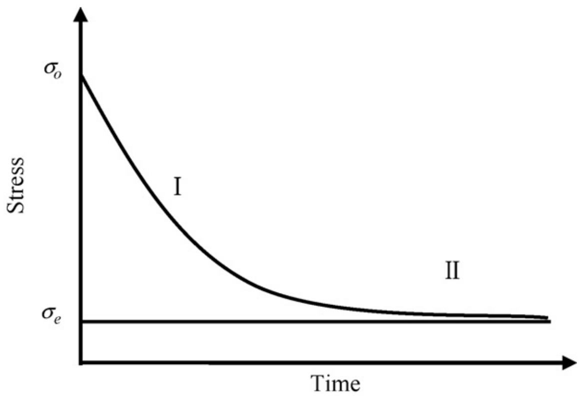

Fig. 1. The schematic diagram of the stress relaxation curve.

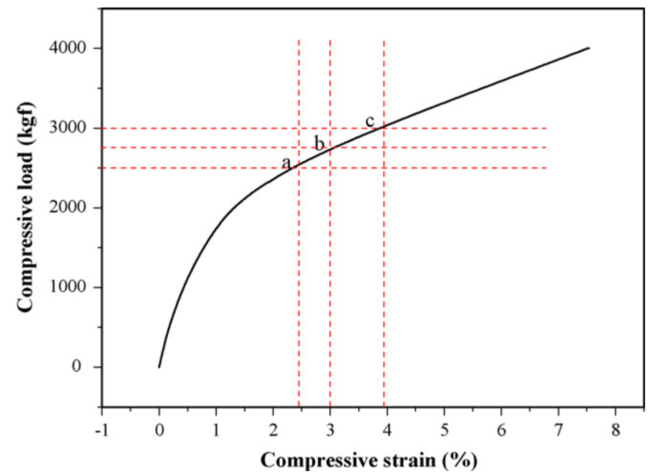

Fig. 3. The compressive load versus strain for the $Fe_{59}Mn_{30}Si_6Cr_5$ alloy.

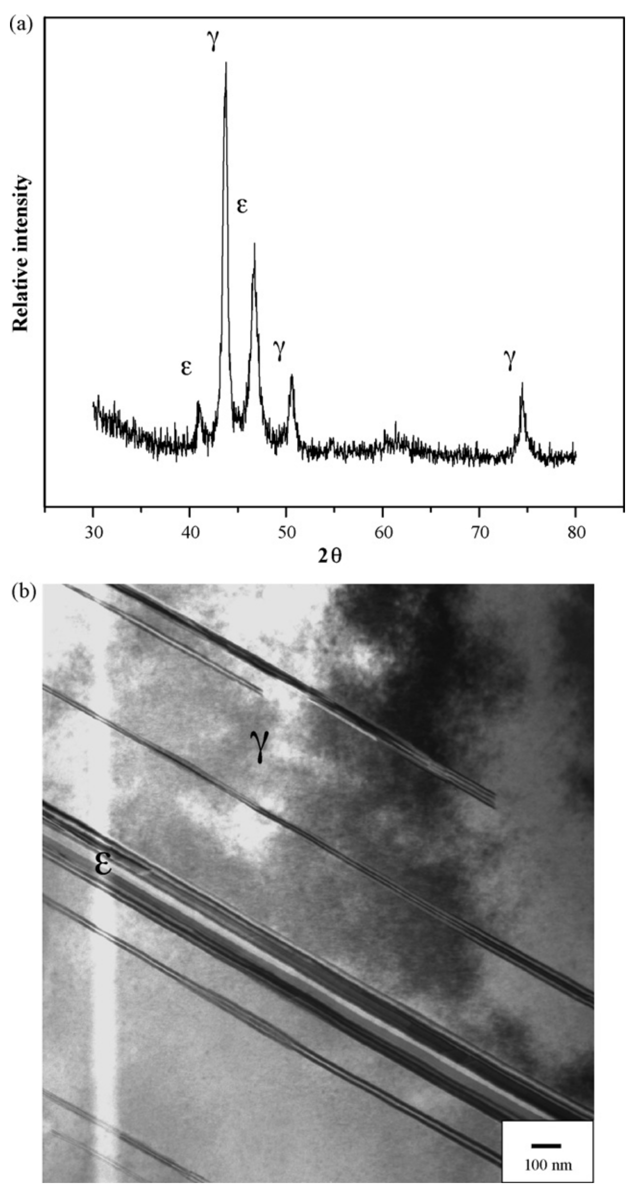

Fig. 2. (a) XRD pattern and (b) TEM observation at room temperature for the as-annealed $Fe_{59}Mn_{30}Si_6Cr_5$ alloy.

relaxation were carried out on a multi-functional MTS (Model: CY-6040A4, made in Taiwan) tester equipped with a heating furnace. During the stress relaxation with cyclic variation of atmospheric temperature, the specimen was set to sustain a constant strain and subjected to the repetition of temperature variation, 1 h at room temperature, followed by a subsequent heating to a set high temperature for 10 min and then cooled to room temperature again. The data were automatically recorded, and stress–strain curves were then calculated from the raw data. The transformation temperatures of this alloy were measured by using a technique of four-probe electrical resistivity. The shape memory effect for the pre-strained specimen, in a state of stress relief, was automatically calculated from the data of recovery strain on heating to a setting temperature. The XRD analysis was carried out at room temperature using a Philips PW1710 X-ray diffractometer with Cu Kα radiation, 30 kV tube voltage, and 20 mA current. The specimens for transmission electron microscope (TEM) were prepared by jet electro-polishing at −25 °C with an electrolyte consisting of 3% $HClO_4$ and 97% C_2H_5OH by volume. TEM observation was carried out by using a JEOL-2000 EX microscope at an operating voltage of 200 kV.

Fig. 1 shows the schematic diagram of the stress relaxation. The initial stress (σ_o) decreases rapidly in region I, and then gradually approaches to a relaxation limit (σ_e) in region II. The amount of stress relaxation is defined as Eq. (1).

$$\text{Relaxation}\,(\%) = \frac{\sigma_o - \sigma_e}{\sigma_o} \times 100 \qquad (1)$$

3. Results and discussion

3.1. Basic properties for $Fe_{59}Mn_{30}Si_6Cr_5$ alloy

Fig. 2(a) and (b) shows the XRD pattern and TEM observation at room temperature for the as-annealed $Fe_{59}Mn_{30}Si_6Cr_5$ alloy. The M_s, M_f, A_s and A_f temperatures for this alloy have been measured to be about 32, −56, 160 and 245 °C, respectively. Hence, the γ and ε phases coexist within the alloy at room temperature, as presented in the XRD patterns of Fig. 2(a). The coexistence

Table 1
The engineering stress and strain for the testing specimens with various compressive loads

Load (kgf)	Stress (kgf/mm^2)	Strain (%)
2500	31.83	2.4
2700	35.01	3.0
3000	38.20	3.9

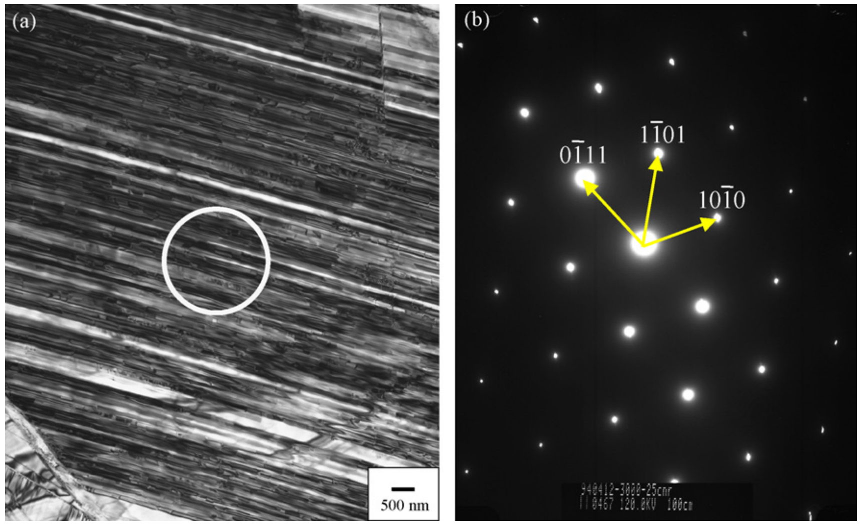

Fig. 4. (a) TEM bright field image and (b) SADP of the specimen subjected to a compressive loading of 3000 kgf at room temperature.

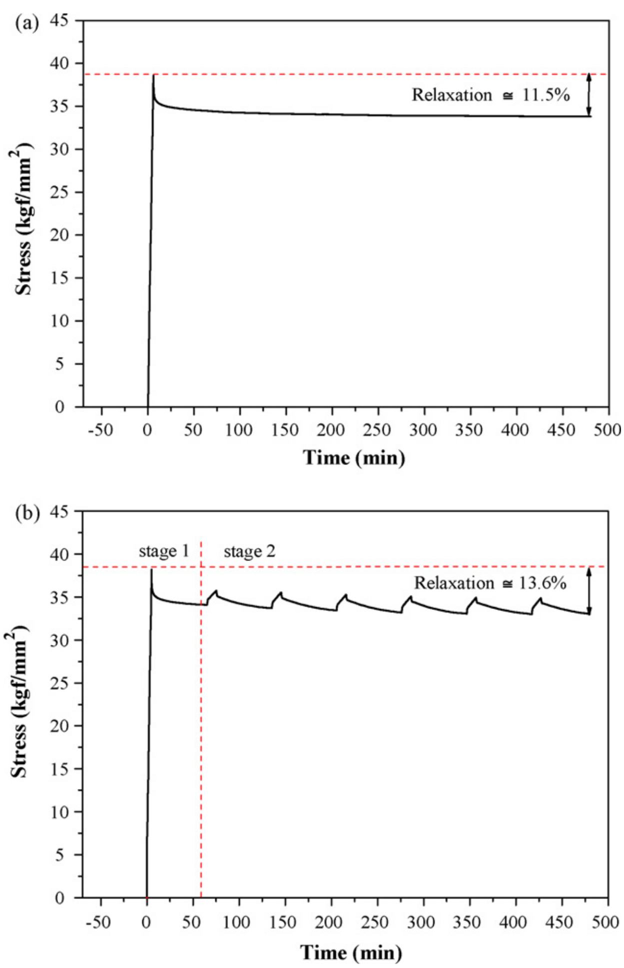

Fig. 5. (a) The static-constrained stress relaxation curve with an initial 3000 kgf loading at room temperature, and (b) the thermal-cycled stress relaxation curve with an initial 3000 kgf loading and 6 times of cyclic heating to 260 °C, for the $Fe_{59}Mn_{30}Si_6Cr_5$ alloy.

of γ and ε phases within the alloy can also be clearly observed in the TEM observation in Fig. 2(b) for the $Fe_{59}Mn_{30}Si_6Cr_5$ specimen. It is known that the pre-strained specimens will exhibit a shape memory effect if they are heated up to a temperature higher than A_s (or even A_f). This shape memory effect is considered to have some influence on the thermal-cycled stress relaxation. In this study, the heating temperatures are 170, 260 and 360 °C (as discussed later), which are around or slightly above the A_s and A_f temperatures. The shape-recovery ratios for the specimens with 2–4% pre-strains are measured to be about 10, 25 and 60% on heating up to 170, 260 and 360 °C, respectively.

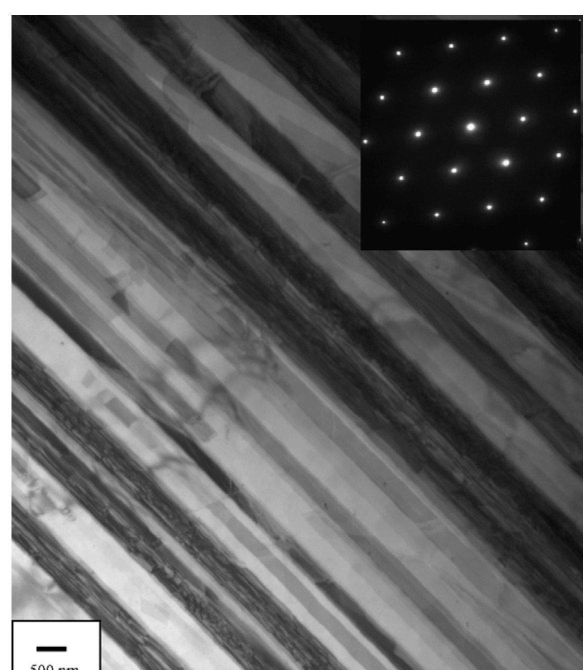

Fig. 6. TEM bright field image of the specimen with a long-time sustaining of 3000 kgf loading at room temperature.

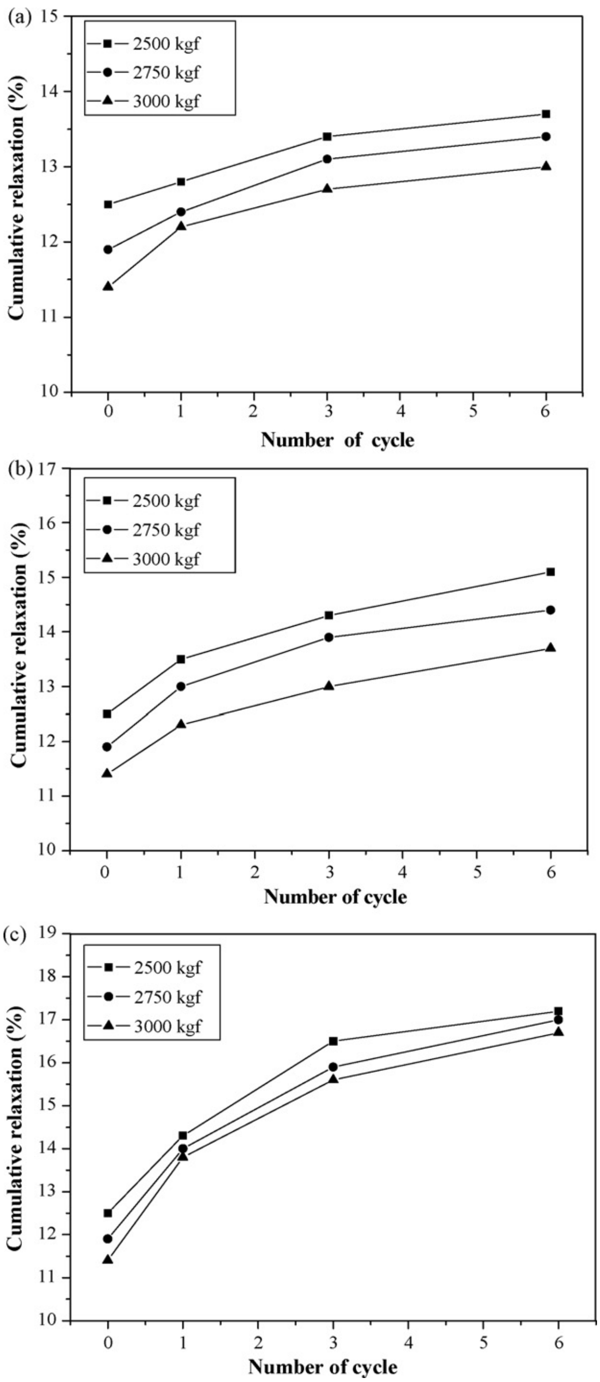

Fig. 7. The cumulative relaxation at various initial loadings versus cyclic number with heating temperatures of (a) 170 °C, (b) 260 °C and (c) 360 °C.

3.2. Static-constrained and thermal-cycled stress relaxation

Fig. 3 shows the compressive load versus strain for the $Fe_{59}Mn_{30}Si_6Cr_5$ alloy. It is known that the recoverable strain of the polycrystalline $Fe_{59}Mn_{30}Si_6Cr_5$ alloy is about 2–4%. Hence, the constrained strains for the experiments of stress relaxation are set to be in the range of 2–4%, as indicated by a, b, and c in Fig. 3. The compressive loads, engineering stresses and strains for these points are presented in Table 1. Meanwhile, the elastic and plastic deformations are found to occur simultaneously in the stress region of a, b, and c. The plastic deformation can be introduced by both stress-induced martensitic transformation and dislocation movement. Fig. 4(a) and (b) shows the TEM bright field image and SADP, respectively, of the specimen subjected to a compressive loading of 3000 kgf at room temperature. As can be seen in Fig. 4(a), many dense and thin platelets of ε martensite appear within the deformed specimen. Based on the analysis of SADP in Fig. 4(b), these thin platelets of ε martensite exhibit a HCP structure.

As mentioned in Section 1, the relaxation phenomena may arise from both the static-constrained stress relaxation (with long-time sustaining of constrained stress) and thermal-cycled stress relaxation (with constrained stress and cyclic variation of atmospheric temperature). Fig. 5(a) and (b) shows the static-constrained stress relaxation curve with an initial 3000 kgf loading at room temperature, and the thermal-cycled stress relaxation curve with an initial 3000 kgf loading and 6 times of cyclic heating to 260 °C, respectively, for the $Fe_{59}Mn_{30}Si_6Cr_5$ alloy. Fig. 5(a) shows a typical curve of static-constrained stress relaxation, namely, and the limit of static-constrained stress relaxation is about 11.5% for the 3000 kgf loading.

Fig. 6 shows the TEM bright field image of the specimen with a long-time sustaining of 3000 kgf loading at room temperature. Compared to Fig. 4(a), the thin platelets of ε martensite have accommodatingly combined to be thicker ones after the stress relaxation during the long-time sustaining. This indicates that the static-constrained stress relaxation may be ascribed to the combination of stress-induced thin platelets of ε martensite. Meanwhile, the platelets of ε martensite will also rearrange to accommodate the constrained loading, and hence the constrained stress is reduced after a long-time sustaining.

In Fig. 5(b), the thermal-cycled stress relaxation can be divided into two stages. In the first stage, the stress relaxation is mainly contributed from the static-constrained relaxation, which is related to the initial loading. As can be seen from Fig. 5(a), the static-constrained stress relaxation completes more than 90% within 30 min. Therefore, in stage 2, the stress relaxation is

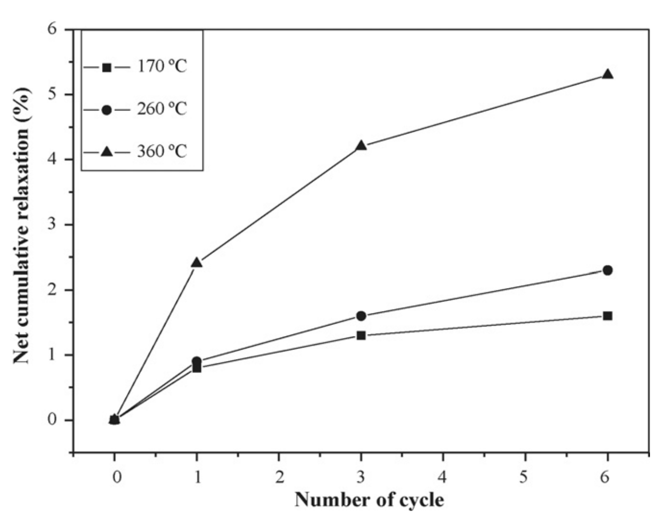

Fig. 8. The net cumulative cyclic relaxation versus cyclic number for specimens with 3000 kgf loading and cyclic heating temperatures of 170, 260 and 360 °C.

mainly associated with the effect of cyclic variation of atmospheric temperature, although the relaxation value is small and is related to the cyclic heating temperature and cyclic number. In the real application of pipe coupling, both long-time sustaining of constrained stress and cyclic variation of atmospheric temperature must occur at the same time. Hence, the following part of this paper will mainly discuss the phenomena of thermal-cycled stress relaxation of the $Fe_{59}Mn_{30}Si_6Cr_5$ alloy, which involves simultaneously both contributions of static-constrained stress and cyclic variation of atmospheric temperature.

3.3. The effect of initial loading and cyclic heating temperature

Fig. 7(a)–(c) shows the cumulative relaxation at various initial loadings versus cyclic number with heating temperatures of 170, 260 and 360 °C, respectively. The temperatures between 170 and 360 °C, being around and slightly above the $\varepsilon \rightarrow \gamma$ transformation temperatures, were selected as the heating temperatures in this study. In Fig. 7(a)–(c), one can find that the cumulative relaxation decreases with increasing initial loadings, namely, 3000 kgf < 2750 kgf < 2500 kgf. This feature can be explained as below. As presented in Table 1, the engineering strains under the loading of 3000, 2750 and 2500 kgf are 3.9, 3.0 and 2.4%, respectively. Fig. 3 also indicates that the ratio of elastic strain/plastic strain under higher loading is smaller than that under lower loading. Hence, less amount of elastic strain under higher loading will be transferred to plastic strain by internal accommodation during the stress relaxation. These accommodation mechanisms may involve the vacancy diffusion, newly formation of ε martensite and movement of martensite/austenite interfaces. In Fig. 7(a)–(c), one can also find that the relaxation phenomenon is more obvious in the earlier cycles and then gradually approaches to a saturated value. Besides, there occurs a higher cumulative relaxation at a higher cyclic heating temperature.

To understand the effect of cyclic heating temperature, the net cumulative relaxation versus cyclic number for specimens with 3000 kgf loading and cyclic heating temperatures of 170, 260 and 360 °C are plotted in Fig. 8. The net cumulative relaxation

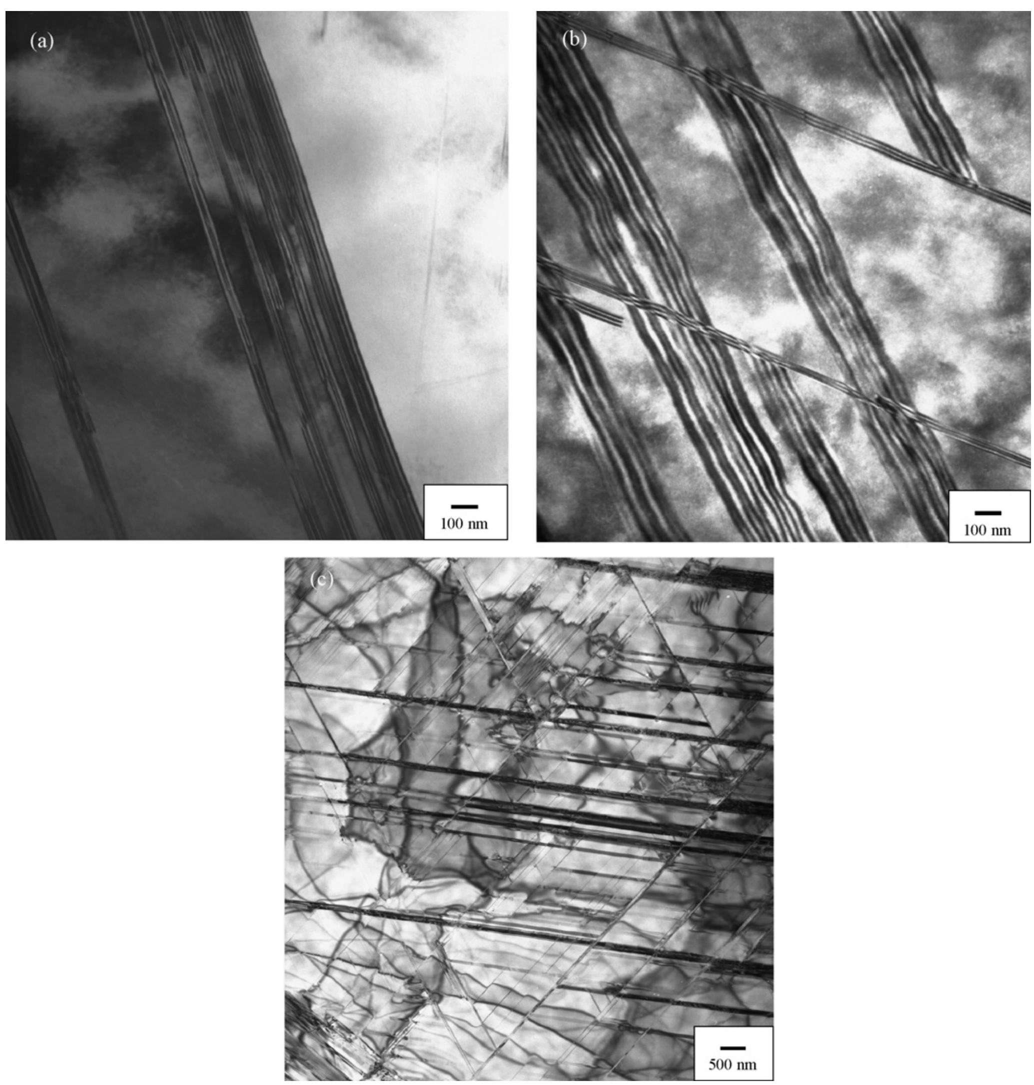

Fig. 9. TEM bright field images for the specimens subjected to an initial 3000 kgf loading at room temperature, being kept the strain and then a heating cycle to (a) 170 °C, (b) 260 °C and (c) 360 °C.

is related only to the cyclic variation of atmospheric temperature and is calculated by deducting 11.5% (the static-constrained relaxation at room temperature) from the total cumulative relaxation. As shown in Fig. 8, the net cyclic relaxation with 6 times of thermal cycling is only 5.2% at a heating temperature of 360 °C, and even less than 2.1% at 260 and 170 °C. This indicates that the cyclic variation of atmospheric temperature has a smaller effect on the relaxation than the static-constrained stress.

Fig. 9(a)–(c) shows the TEM bright field images for the specimens subjected to an initial 3000 kgf loading at room temperature, being kept the strain and then a heating cycle to 170, 260 and 360 °C for 10 min, respectively. As clearly shown in Fig. 9(b) and (c), in addition to the preferential platelets of ε martensite, there appear other groups of ε martensite with different orientations. The more the thermal cycling, the more the quantity of the other groups of ε martensite, as shown in Fig. 10 for the same specimens as Fig. 9(a)–(c), but now with 6 times of thermal cycling. The TEM observations demonstrate that the effect of cyclic heating on the stress relaxation originates mainly from the formation of new-oriented ε martensite. This feature is believed to be related to the reverse transformation of $\varepsilon \rightarrow \gamma$ during heating and the forward transformation of $\gamma \rightarrow \varepsilon$ during the following cooling process. Meanwhile, the thermal stress and shape-recovery stress (due to the shape memory effect) under the fixed constrained strain during the heating process will also be expected to enhance the formation of new-oriented ε martensite. At a lower cyclic heating temperature of 170 °C, which is slightly above the A_s temperature, only a small part of $\varepsilon \rightarrow \gamma$ transformation can occur during the heating process. Hence, no obvious new-oriented ε martensite can be observed after the cyclic heating, as shown in Figs. 9(a) and 10(a). With increasing the cyclic heating temperature to 260 and 360 °C, which are higher than the A_f temperature, more thermal stress and shape-recovery stress during the cyclic heating process will enhance the formation of new-oriented ε martensite, as shown in Figs. 9(b and c) and 10(b and c). It is worthy to mention

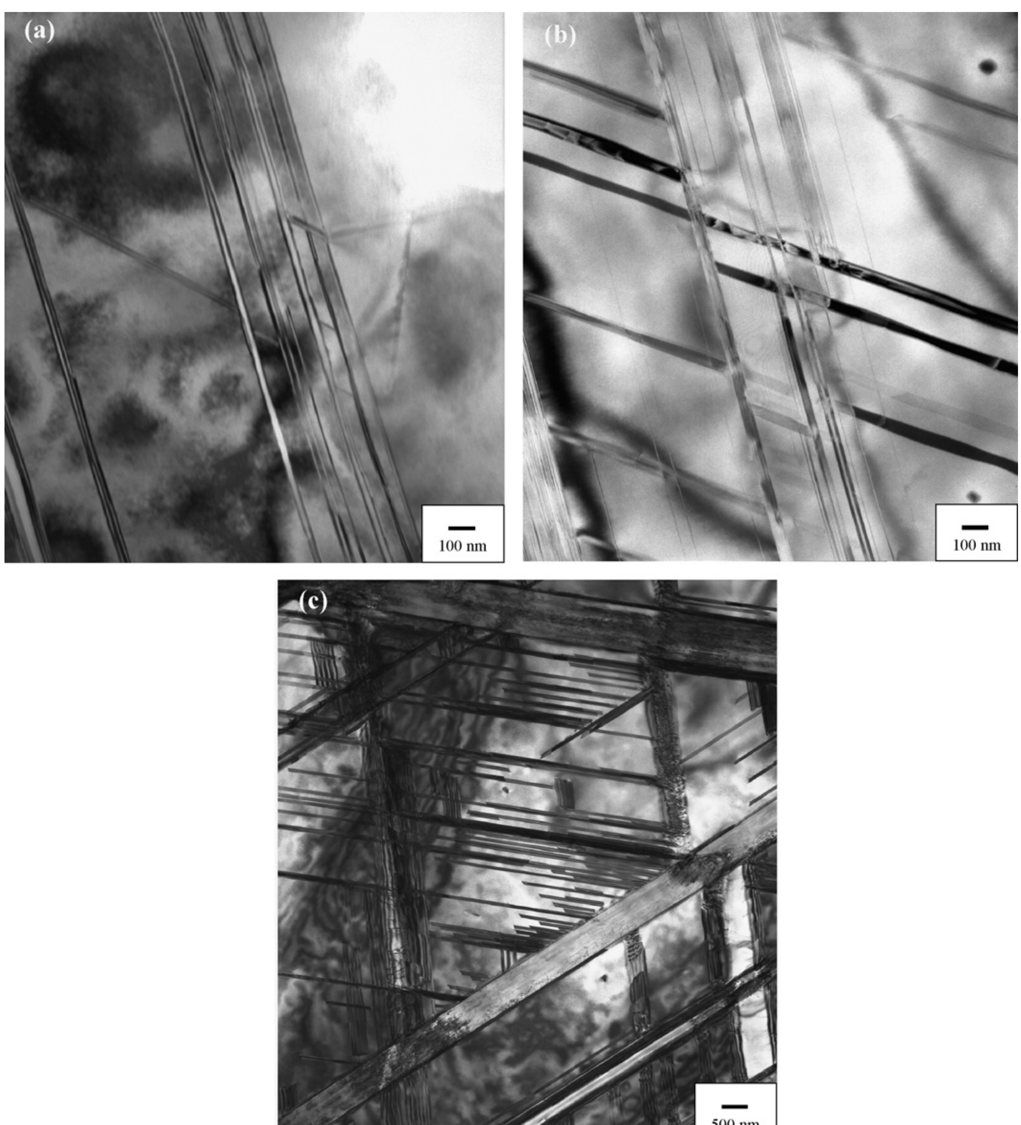

Fig. 10. TEM bright field images of the same specimens as Fig. 9(a–c), but now they have been subjected to 6 times of thermal cycling.

that the net relaxation amount per cycle decreases gradually with increasing cyclic number, as shown in Fig. 8. This indicates that the formation rate of new-oriented ε martensite will decrease with increasing cyclic number. This feature is reasonable because the formation of new-oriented ε martensite will be more difficult in the later thermal cycles.

It is interesting to compare the stress relaxation of this Fe–Mn–Si–Cr shape memory alloy to other metals and alloys. In general, the stress relaxation of metals and alloys is due to the viscous flow at elevated temperature [23–26], including the vacancy diffusion, grain boundary sliding and dislocation creep. Meanwhile, the an-elastic behavior [27], such as carbon diffusion in BCC iron under stress state, will also exhibit a phenomenon of stress relaxation. In the present study, the Fe–Mn–Si–Cr alloy can exhibit a stress-induced $\gamma \rightarrow \varepsilon$ transformation and a reverse $\varepsilon \rightarrow \gamma$ transformation on heating process. As mentioned above, the mechanism of stress relaxation for this alloy are mainly due to the accommodating combination of ε platelets and the formation of new-oriented ε martensite. This mechanism is similar to that reported for sputtered shape memory TiNi film, in which the residual stress existing within the film can be partially relaxed due to the reversible martensitic transformation [28].

4. Conclusions

The stress relaxation of $Fe_{59}Mn_{30}Si_6Cr_5$ shape memory alloy was studied by using a compressive test. The important conclusions are as follows:

1. At higher initial loading, small amount of elastic strain will be transferred to plastic strain by internal accommodation. Hence, the relaxation amount decreases with increasing initial loading.
2. The cyclic variation of atmospheric temperature has a smaller effect on the relaxation than the static-constrained stress. A higher amount of relaxation occurs at a higher cyclic heating temperature. The relaxation phenomenon is more obvious in the earlier cycles and then gradually approaches to a saturated value.
3. The static-constrained stress relaxation is ascribed to the combination of stress-induced thin platelets of ε martensite. The platelets of ε martensite will also rearrange to accommodate the constrained loading, and hence the constrained stress is reduced.
4. The effect of cyclic heating on the stress relaxation is originated from the formation of new-oriented ε martensite. The $\varepsilon \leftrightarrow \gamma$ transformation, thermal stress and shape-recovery stress during the thermal cycling are considered to have significant influences on the formation of new-oriented ε martensite.

Acknowledgements

The authors would like to sincerely acknowledge the financial support of this study by Taiwan Textile Research Institute and National Science Council (NSC), Republic of China, under Grant No. NSC 93-2216-E-002-025.

References

[1] A. Sato, E. Chishima, K. Soma, T. Mori, Acta Metall. 30 (1982) 1177.
[2] A. Sato, E. Chishima, Y. Yamaji, T. Mori, Acta Metall. 32 (1984) 539.
[3] A. Sato, K. Soma, E. Chishima, T. Mori, J. Phys. (1982), C4-797.
[4] M. Murakami, H. Otsuka, H. Suzuki, S. Matsuda, Trans. ISIJ 27 (1987) B–88.
[5] X.X. Wang, L.C. Zhao, Scripta Metall. Mater. 26 (1992) 1451.
[6] L. Federzoni, G. Guenin, Scripta Metall. Mater. 31 (1994) 25.
[7] H.C. Lin, K.M. Lin, Scripta Metall. Mater. 34 (1996) 343.
[8] H.C. Lin, K.M. Lin, T.S. Chou, Scripta Metall. Mater. 35 (1996) 879.
[9] M. Sade, K. Halter, E. Hornbogen, Z. Metallkd. 79 (1988) 487.
[10] A. Sato, Y. Yamaji, T. Mori, Acta Metall. 34 (1986) 287.
[11] K. Tsuzaki, M. Ikegami, Y. Tomota, T. Maki, ISIJ 30 (1990) 666.
[12] B.H. Jiang, T. Tadaki, H. Mori, T.Y. Hsu, Mat. Trans. JIM 38 (1997) 1072.
[13] B.H. Jiang, X.A. Qi, W.M. Zhou, Z.L. Xi, T.Y. Hsu, Scripta Metall. Mater. 34 (1996) 1437.
[14] R.D. Xia, G.W. Liu, T. Liu, Mater. Lett. 32 (1997) 131.
[15] T. Maki, I. Tamura, Proc. ICOMAT-86 (1986) 963.
[16] M. Murakami, H. Otsuka, G. Suzuki, M. Masuda, Proc. ICOMAT-86 (1986) 985.
[17] A. Sato, K. Takagaki, S. Horie, M. Kato, T. Mori, Proc. ICOMAT-86 (1986) 979.
[18] O. Soderberg, X.W. Liu, P.G. Yakovenko, K. Ullakko, V.K. Lindroos, Mater. Sci. Eng. A 273–275 (1999) 543.
[19] V.V. Bliznuk, V.G. Gavriljuk, B.D. Shanina, A.A. Konchits, S.P. Kolesnik, Acta Mater. 51 (2003) 6095.
[20] J.C. Li, W. Zheng, Q. Jiang, Mater. Lett. 38 (1999) 275.
[21] H. Kubo, K. Nakamura, S. Farjami, T. Maruyama, Mater. Sci. Eng. A 378 (2004) 343.
[22] H. Tanahashi, T. Maruyama, H. Kubo, Trans. Mat. Soc. Jpn. 18B (1994) 1149.
[23] L. Xiao, J.L. Bai, Mater. Sci. Eng. A 244 (1998) 250.
[24] P. Juijerm, I. Altenberger, Scripta Mater. 55 (2006) 1111.
[25] Z. Drozd, Z. Trojanova, S. Kudela, Mater. Sci. Eng. A 462 (2007) 234.
[26] Thomas H. Courtney, Mechanical Behavior of Materials, second ed., 2000 (Chapter 7).
[27] Robert E. Reed-Hill, Reza Abbaschian, Physical Metallurgy Principles, third ed., 1994 (Chapter 13).
[28] Y. Fu, H. Du, Surf. Coat. Technol. 153 (2002) 100.